Ce3+:Lu3Al5O12–Al2O3 optical nanoceramic scintillators elaborated via a low-temperature glass crystallization route

Jie Fu, Shaowei Feng, Yongchang Guo, Ying Zhang, Cécile Genevois, Emmanuel Veron, Mathieu Allix, Jianqiang Li

Journal of Advanced Ceramics
2023, **12**(2): 268–278
https://doi.org/10.26599/JAC.2023.9220681
ISSN 2226-4108
CN 10-1154/TQ

Research Article

Ce^{3+}:$Lu_3Al_5O_{12}$–Al_2O_3 optical nanoceramic scintillators elaborated via a low-temperature glass crystallization route

Jie FU[a,b,d], Shaowei FENG[b,d], Yongchang GUO[b,d], Ying ZHANG[b,d], Cécile GENEVOIS[c], Emmanuel VERON[c], Mathieu ALLIX[c,*], Jianqiang LI[a,*]

[a]*School of Materials Science and Engineering, University of Science and Technology Beijing, Beijing 100083, China*
[b]*State Key Laboratory of Multiphase Complex Systems, Institute of Process Engineering, Chinese Academy of Sciences, Beijing 100190, China*
[c]*CNRS, CEMHTI UPR 3079, Université d'Orléans, Orléans 45071, France*
[d]*University of Chinese Academy of Sciences, Beijing 100049, China*

Received: June 23, 2022; Revised: October 1, 2022; Accepted: October 18, 2022

Abstract: Transparent Ce:lutetium aluminum garnet (Ce:$Lu_3Al_5O_{12}$, Ce:LuAG) ceramics have been regarded as potential scintillator materials due to their relatively high density and atomic number (Z_{eff}). However, the current Ce:LuAG ceramics exhibit a light yield much lower than the expected theoretical value due to the inevitable presence of Lu_{Al} antisite defects at high sintering temperatures. This work demonstrates a low-temperature (1100 ℃) synthetic strategy for elaborating transparent LuAG–Al_2O_3 nanoceramics through the crystallization of 72 mol% Al_2O_3–28 mol% Lu_2O_3 (ALu28) bulk glass. The biphasic nanostructure composed of LuAG and Al_2O_3 nanocrystals makes up the whole ceramic materials. Most of Al_2O_3 is distributed among LuAG grains, and the rest is present inside the LuAG grains. Fully dense biphasic LuAG–Al_2O_3 nanoceramics are highly transparent from the visible region to mid-infrared (MIR) region, and particularly the transmittance reaches 82% at 780 nm. Moreover, Lu_{Al} antisite defect-related centers are completely undetectable in X-ray excited luminescence (XEL) spectra of Ce:LuAG–Al_2O_3 nanoceramics with 0.3–1.0 at% Ce. The light yield of 0.3 at% Ce:LuAG–Al_2O_3 nanoceramics is estimated to be 20,000 ph/MeV with short 1 μs shaping time, which is far superior to that of commercial $Bi_4Ge_3O_{12}$ (BGO) single crystals. These results show that a low-temperature glass crystallization route provides an alternative approach for eliminating the antisite defects in LuAG-based ceramics, and is promising to produce garnet-based ceramic materials with excellent properties, thereby meeting the demands of advanced scintillation applications.

Keywords: glass crystallization; garnet antisite defects; $Lu_3Al_5O_{12}$–Al_2O_3 (LuAG–Al_2O_3) transparent ceramics; nanoceramics; scintillation

* Corresponding authors.
E-mail: J. Li, jianqiangli@ustb.edu.cn;
M. Allix, mathieu.allix@cnrs-orleans.fr

1 Introduction

Scintillation materials play irreplaceable roles in many applications including modern medical imaging, high-energy physics, and security inspection [1–3]. Lutetium aluminum garnet ($Lu_3Al_5O_{12}$, LuAG) is recognized as a promising scintillation matrix material on account of its relatively high density of 6.7 g/cm^3 and high atomic number (Z_{eff} = 63) [4]. LuAG crystals doped with Pr^{3+} or Ce^{3+} have made themselves attractive on account of featuring characteristics of fast scintillation response of about 50 ns, high light yield exceeding 25,000 ph/MeV, and high energy resolution approaching 5% at 662 keV [4–7]. Unfortunately, some insurmountable drawbacks, such as high production costs, time-consuming production periods, and low segregation coefficients of rare earth ions, give rise to the restricted industrialization of single crystals [8]. In the last few decades, transparent ceramics have gained instant attention due to the apparent advantages over the single crystals in the aspects of a synthetic process (short production periods and low costs) and product characteristics (large volume, structural diversity, and doping flexibility) [8–10]. Moreover, transparent ceramic scintillators have proved their ability to compete with the single crystal scintillators in numerous domains, especially in X-ray computed tomography (X-CT) [11,12]. It is reported that Ce:LuAG and Pr:LuAG transparent ceramic materials with light yields exceeding those of the single crystals have been successfully synthesized in the past ten years [13,14]. Multicomponent LuAG-based transparent ceramics, such as Pr:$(Lu_{0.75}Y_{0.25})_3Al_5O_{12}$ (Pr:LuYAG) [15] and Ce:$(Gd,Lu)_3Ga_3Al_2O_{12}$ (Ce:GLuGAG) [16] with light yields of 24,000–50,000 ph/MeV have also been considered as competitive candidates for diverse scintillation applications.

Even so, the reported light yields of the LuAG single crystals and ceramics are well below their theoretical limit of 60,000 ph/MeV [17]. Nikl *et al*. [18] confirmed the existence of Lu_{Al} antisite defects and its trap depth of 0.29 eV in Ce:LuAG by low-temperature thermally stimulated luminescence (TSL). This shallow electron trap can easily capture carriers during the carrier transport process, delay the energy transport to the Ce^{3+}/Pr^{3+} emission center, and thereby severely deteriorate scintillation characteristics of the LuAG single crystals and ceramics [4,19]. The elimination or suppression of the antisite defects in the garnet scintillators has attracted extensive attention in relevant studies [19–21]. The defect engineering represented by Mg co-doping and the bandgap engineering represented by Ga^{3+} and Gd^{3+} introductions are recognized as effective approaches to suppress and eliminate the antisite defects in the garnet-based ceramics. It has been demonstrated that Mg^{2+} co-dopants in the LuAG ceramics are able to drive the partial conversion of Ce^{3+} to Ce^{4+} [22,23]. The Ce^{4+} center possesses the capability to positively influence the scintillation process by acting as precursors of temporary Ce^{3+} centers and working in parallel with stable Ce^{3+} centers, thereby forming the Ce,Mg:LuAG optical ceramic materials with a light yield of up to 25,000 ph/MeV [23]. Besides, a balanced admixture of Gd^{3+} and Ga^{3+} has brought about a breakthrough in the scintillation property of the garnet structure, and the high light yield even exceeds the theoretical limit of 60,000 ph/MeV [24].

Besides, Zorenko *et al*. [25,26] demonstrated that very high preparation temperatures, especially high melt crystallization temperatures (1800–1900 ℃) for the single crystal, are highly conducive to Lu^{3+} ions, entering the Al^{3+} lattice site to form Lu_{Al} antisite defects. Therefore, reducing the preparation temperature while retaining good cristallinity is considered to be a promising parameter to restrain the generation of the antisite defects. The elaboration of the transparent garnet-based ceramics is currently employing powder sintering routes including vacuum sintering [27–29], hot isostatic pressing [30,31], and spark plasma sintering [32]. On the one hand, the antisite defects still ineluctably appear in the as-sintered ceramics due to the high sintering temperatures. For instance, although the Mg^{2+} introduction played a role in lowering the TSL spectra intensity, especially below 127 ℃, there are still some shallow traps existing in the LuAG transparent ceramics prepared by vacuum sintering at 1850 ℃ for 10–30 h followed by annealing at 1450 ℃ for 20 h [23]. Thus, a low-temperature synthesis solution was desirable to suppress the generation of the Lu_{Al} antisite defects. On the other hand, high-quality (such as high-purity, good-dispersibility, and nano-sized) raw material powders are indispensable in such powder sintering routes to ensure the absence of scattering centers including impurities and pores, to harvest the ceramic materials with high transparency [10,33].

Recently, the crystallization from the bulk glass has been recognized as a novel approach to reap the fully dense transparent polycrystalline ceramics at lower

temperatures (usually not more than 1100 ℃) [34]. Alahraché *et al*. [35] elaborated $Sr_{1+x/2}Al_{2+x}Si_{2-x}O_8$ ($0 < x \leqslant 0.4$) transparent ceramics through the full and congruent crystallization of the glass derived from melt quenching in rhodium/platinum crucibles. Besides, they also developed a series of transparent ceramic materials including $BaAl_4O_7$ [36], $Ln_{1+x}Sr_{1-x}Ga_3O_{7+\delta}$ (Ln = Eu, Gd, or Tb) [37], and $La_{1+x}Ca_{1-x}Al_3O_{7+0.5x}$ (x = 0–0.5) [38] through the full crystallization of the glass solidified by aerodynamic levitation furnaces. In Refs. [39,40], YAG-based transparent nanoceramic materials with excellent optical and mechanical properties were elaborated at 963 and 1100 ℃ by pressureless full crystallization from the 74 mol% Al_2O_3–26 mol% Y_2O_3 (AY26) bulk glass raised by the containerless solidification process. Thus, the low-temperature glass crystallization technology is a worth-trying synthesis route to avoid the antisite defects in the LuAG-based transparent ceramic materials. As yet, there is no report on the fabrication of the LuAG-based transparent ceramics via such low-temperature glass crystallization process.

In this work, highly transparent LuAG–Al_2O_3 nanoceramics were elaborated through the pressureless crystallization from the 72 mol% Al_2O_3–28 mol% Lu_2O_3 (ALu28) bulk glass, whose composition deviates from the stoichiometric LuAG. The scintillation properties of the LuAG-based nanoceramics with Ce concentrations varying from 0.1 to 1.0 at% were investigated. Especially, the existence of shallow and deep defects in the LuAG-based nanoceramics was examined and discussed in detail. The results show that the low-temperature glass crystallization route has a positive effect on suppressing and reducing the Lu_{Al} antisite defects in the LuAG-based transparent ceramics.

2 Experimental

2. 1 Sample preparation

The commercial oxide powders of 99.99% purity were purchased from Sinopharm Chemical Reagent Co., Ltd. (Al_2O_3 and CeO_2) and Qiandong Rare Earth Group Co., Ltd. (Lu_2O_3). According to the composition of 72 mol% Al_2O_3–28 mol% ($(1-x)Lu_2O_3$,$2xCeO_2$) (x = 0, 0.001, 0.003, 0.005, 0.008, and 0.01), the raw material powders were weighed, mixed in an agate mortar using ethanol as a dispersant, and dried at 50 ℃ in an air drying oven. The mixed powders were pressed into pellets with a mass of 0.05–0.20 g and placed in an aerodynamic levitation furnace coupled with CO_2 laser heating. A transparent glass bead was fabricated by heating a pellet at ~2800 ℃ for 10–30 s followed by rapid quenching at a cooling rate of ~300 ℃/s by turning off the laser heating. As reported in Refs. [39,40], these bulk glass precursors were heated at 950–1300 ℃ for 2 h to perform full crystallization, i.e., to produce the transparent ceramics.

2. 2 Characterization

The phase compositions and crystallinities of the as-prepared samples were investigated by a high-resolution X-ray diffractometer (XRD; Empyrean, PANalytical B.V., the Netherlands) running with Cu-Kα radiation (1.5406 Å). The data were collected at room temperature from 2θ = 10° to 130° with a 0.013° step size at a voltage of 45 mV and a current of 40 mA. Thermal analysis of the glass samples was determined by a differential scanning calorimeter (DSC; MULTI HTC 1600, SETARAM, France) from room temperature to 1200 ℃ using argon as purging gas, and the heating rate was 10 ℃/min. The densities of the synthesized samples were measured by a density test system of an electronic balance (ME204, METTLER TOLEDO). The test samples were polished on both sides, and the dimension of the test samples was ϕ3 mm × 1 mm in thickness. Archimedes' principle was the principle of this density test. Crystallite sizes of the samples were obtained from X-ray powder diffraction (XRPD) results by full spectrum fitting using Rietveld's method. A computer program was used to fit the calculated intensity with the experimental intensity with a certain peak shape function. During the fitting process, the parameters of the structural model and the peak shape function were continuously adjusted to make the calculated peak shape match the observed peak shape; a strain correction factor was added, and thereby the resulting crystal size was corrected. The fitting was performed by the least squares method. The microstructures of the resulting ceramics were observed by a transmission electron microscope (JEM ARM200F FEG, JEOL, Japan). The acquisition of high-resolution transmission electron microscopy (HRTEM) and scanning transmission electron microscopy-high angle annular dark field (STEM-HAADF) images requires mechanical grinding of the samples to a thickness of 50 μm, followed by ion thinning and then observation. Backscattered scanning electron microscopy (SEM) images of the ceramic

samples were observed and analyzed through a scanning electron microscope (JSM-7001F, JEOL, Japan). Optical in-line transmittance of the ceramic materials with a thickness of 1.0 mm was recorded by an ultraviolet–visible–near-infrared (UV–Vis–NIR) spectrophotometer (Cary 5000, Agilent Inc., USA) within a wavelength range of 190–2500 nm and a Fourier-transform infrared spectrometer (Excalibur 3100, Varian Inc., USA) within a wavelength range of 2500–8000 nm. X-ray excited luminescence (XEL) spectra of the obtained ceramic materials were performed on an XEL spectrometer (XJD-100, Dandong Aolong Ray Instrument Group Co., Ltd., China). Regarding the TSL measurements, the samples were irradiated by the X-ray for 10 min at room temperature, and the heating rate of 1.0 ℃/s was adopted. Pulse height spectra were detected by a photomultiplier (PMT; R1306, Hamamatsu, Japan) and recorded by a spectroscopic amplifier under a γ-ray excitation (^{137}Cs source) of 662 keV with shaping time of 1 μs. Gaussian fitting was used to fit the height spectra, and energy resolution was estimated by dividing the full width at half maximum (FWHM) with the number of channels of the Gaussian fitting peaks.

3 Results and discussion

3. 1 Preparation of transparent LuAG–Al_2O_3 nanoceramics

A transparent bulk Lu_2O_3–Al_2O_3 sample (with a diameter of 2.5 mm) consisting of ALu28 is presented in the inset of Fig. S1 in the Electronic Supplementary Material (ESM). The XRPD pattern in Fig. S1 in the ESM shows that the transparent ALu28 sample actually consists of a major glass matrix and a small amount of $LuAlO_3$ crystal phase. Thermal behavior of ALu28 glass-based precursors was analyzed by a differential scanning calorimetry curve, as shown in Fig. 1(a). Glass transition temperature (T_g) showing up at 898 ℃ is followed by a unique and strong exothermic peak temperature (T_p) at 949 ℃ corresponding to the crystallization of the sample. Thus, the heat treatment at 950–1300 ℃, i.e., just above the crystallization temperature, was adopted to crystallize ALu28 glass-based precursors and aim for the transparent ceramic materials. The samples remained transparent up to 1200 ℃ but turned opaque as the heat-treatment temperature reached 1300 ℃.

The XRPD patterns in Fig. 1(b) show that the main diffraction peaks in all transparent materials are highly matched with the pattern of $Lu_3Al_5O_{12}$ (PDF Card No. 73-1368). Some $LuAlO_3$ phases can be clearly observed in the transparent ceramics elaborated at 950 and 1000 ℃, but not in the samples heat-treated at 1100 ℃ or above. In Ref. [39], the transparent ceramics from the full crystallization of the AY26 bulk glass were composed of a YAG main crystal phase and an Al_2O_3 secondary phase. According to the original composition proportion of ALu28 Lu_2O_3, deviating from stoichiometric LuAG (62.5 mol% Al_2O_3–37.5 mol% Lu_2O_3), an Al_2O_3

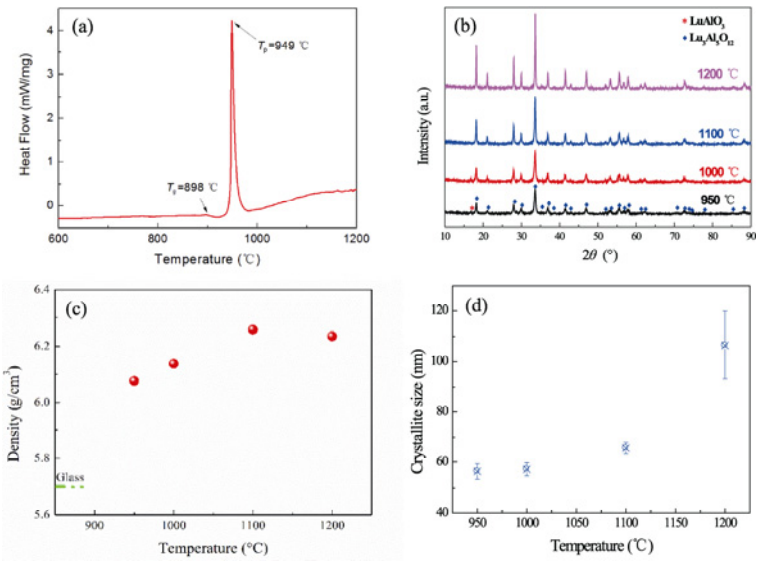

Fig. 1 (a) Differential scanning calorimetry curve of ALu28 glass-based precursors synthesized through containerless solidification process; (b) XRPD patterns, (c) densitiy, and (d) crystallite sizes of transparent materials (1.0 mm in thickness) crystalized from ALu28 glass-based precursors at 950, 1000, 1100, and 1200 ℃ for 2 h.

excess is expected on the side of the LuAG formation. As expected, the Al_2O_3 secondary phase in the ceramics obtained at 1100 ℃ is certified by the XRPD pattern (Fig. 2) coupled with the STEM observation (Fig. 3). Besides, the density of the ALu28 bulk glass-based precursor is only 5.7 g/cm^3, while that is 6.3 g/cm^3 for the transparent ceramics obtained at 1100 ℃, as shown in Fig. 1(c), signifying that a huge volume shrinkage (~10.5%) occurs during the crystallization process of the ALu28 bulk glass-based precursor. When the heat-treated temperature exceeds 1100 ℃, the density of the obtained ceramics barely changes, revealing the completion of the volume shrinkage, which signifies the complete crystallization of LuAG from the ALu28 glass-based precursor. Moreover, the lower density of the resulting ceramics than the theoretical density (6.7 g/cm^3) of LuAG is mainly due to the presence of the Al_2O_3 secondary phase with a low density. Considering strain effect correction, the fitted crystallite sizes are shown in Fig. 1(d). It shows the continuous grain growth of the resulting ceramics with the increase of the crystallization temperature, which is confirmed by the backscattered SEM images (Fig. S2 in the ESM) of the ceramics obtained at 1100 and 1300 ℃. The transparent ceramics with nanocrystalline can be obtained when the crystallization temperature is less than 1100 ℃, which is further supported by the STEM image in Fig. 3(a).

Some Al_2O_3 phases are identified by the diffraction peak of δ-Al_2O_3 in the XRPD pattern in Fig. 2, which demonstrates that LuAG–Al_2O_3 biphasic transparent ceramics are reaped from the crystallization of the ALu28 glass-based precursor at 1100 ℃ for 2 h. Besides, we guess that some transitional Al_2O_3 with low crystallinity, which is difficult to be detected by the XRPD, may also exist in this ceramic. The STEM-HAADF image in Fig. 3(a) clearly shows that the LuAG–Al_2O_3 transparent ceramics are composed of the nanocrystals smaller than 100 nm, which is in keeping with the crystallite size of 65.7±2.3 nm in Fig. 1(d). No pores or microcracks appear in the LuAG–Al_2O_3 nanoceramics, signifying that a fully dense structure is formed in spite of suffering huge volume shrinkage during the glass crystallization process. There are two distinct phases, namely the dark phase and bright phase, which fuse with each other to form the whole ceramic materials. The grains of LuAG appear in a bright area due to the higher average atomic number ($\overline{Z_{LuAG}} \approx 47.6$), and a dark area is composed of the Al_2O_3 grains with a lower average atomic number ($\overline{Z_{Al_2O_3}} \approx 10.6$). Most of Al_2O_3 is distributed among the LuAG grains as intergranular Al_2O_3, and the rest of Al_2O_3 is observed inside the LuAG grains in the form of the intragranular Al_2O_3, as

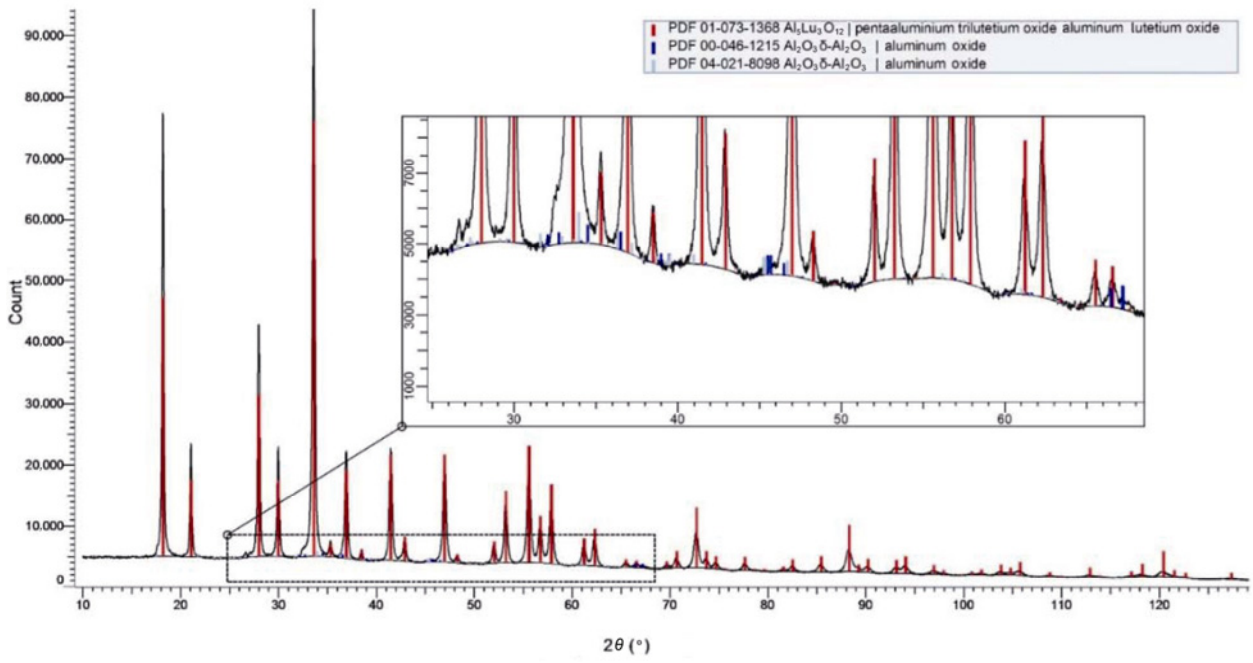

Fig. 2 XRPD pattern of LuAG–Al_2O_3 nanoceramics crystallized from ALu28 glass-based precursor via a 2-h heat treatment at 1100 ℃ in air.

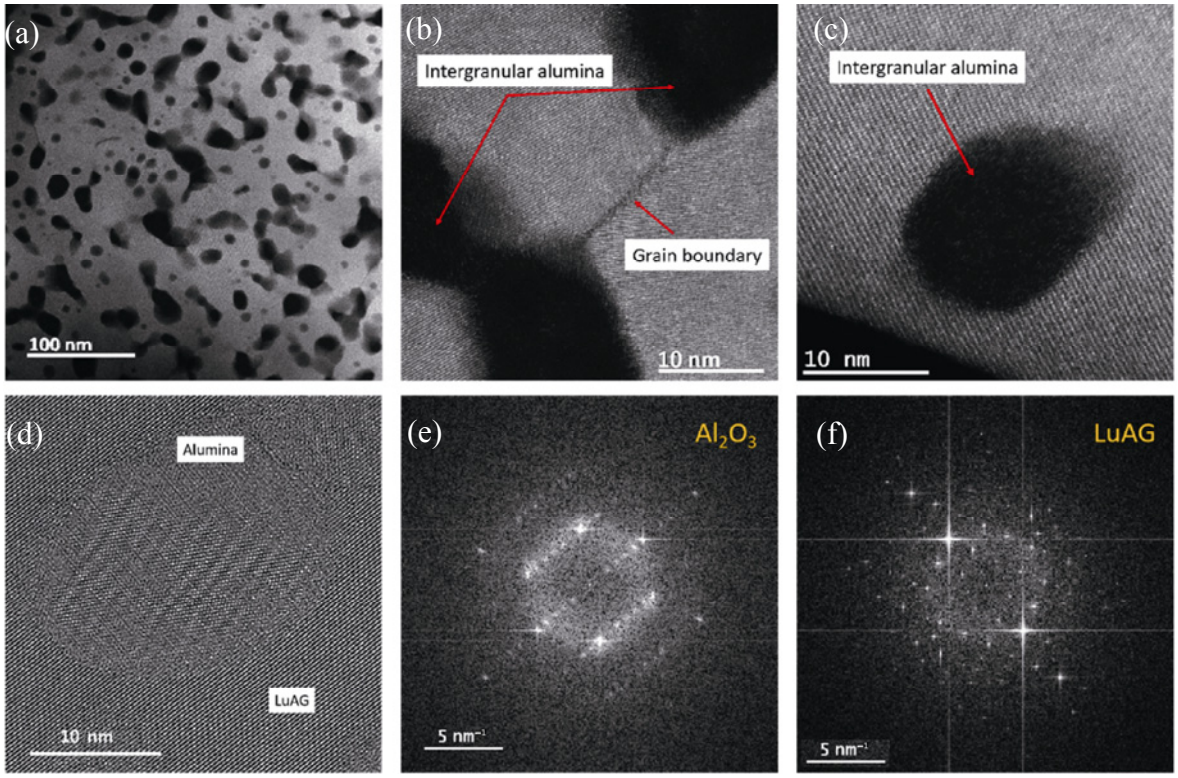

Fig 3 (a–c) STEM-HAADF images; (d–f) HRTEM micrograph and fast Fourier transform (FFT) patterns of LuAG–Al_2O_3 nanoceramics crystallized from ALu28 glass-based precursors (1100 ℃, 2 h).

shown in Figs. 3(b) and 3(c). In Ref. [39], we proposed that nanoscale phase separation may occur upon the crystallization heat treatment of AY26 glass. Likewise, the nanoscale phase separation may also take place prior to the crystallization during the heat treatment of the ALu28 glass-based precursor. The intragranular Al_2O_3 may be a residue of this phase separation. It is not ruled out that this intragranular Al_2O_3 appears during the crystallization process; for example, because the viscosity of the glass is too high, some of the excess Al_2O_3 cannot be expelled (to the future grain boundaries) and must be accommodated. In addition, this may also be due to the coalescence effect of the LuAG grains, which makes Al_2O_3 at the grain boundaries become intragranular. The HRTEM micrograph and FFT patterns in Figs. 3(d)–3(f) show that the network of Al_2O_3 is not so evident compared with that of LuAG; this is related to the slightly poorer crystallinity of Al_2O_3 than that of LuAG, and there is no orientation relationship or cell accommodation between Al_2O_3 and the LuAG grain. The Al_2O_3 layers nailed to the grain boundary have a positive inhibitory effect on restraining the LuAG grain growth rate during the crystallization process, and these LuAG nanocrystals contact each other and together form a unique three-dimensional (3D) network nanostructure. Consequently, the specific LuAG–Al_2O_3 biphasic nanoceramics are elaborated from the crystallization of the ALu28 bulk glass-based precursor at 1100 ℃. Such self-limited growth effect and special biphasic nanostructures have also been observed in Refs. [39,40].

The in-line transmittance of the as-prepared transparent materials (1.0 mm in thickness) crystallized from the ALu28 glass-based precursors at 950, 1000, 1100, and 1200 ℃ for 2 h were measured in the UV–Vis–NIR and mid-infrared (MIR) regions, as shown in Fig. 4. It indicates that the resulting materials show excellent transparency in Vis–NIR and MIR regions. Especially, the transparent ceramics prepared at 1100 ℃ exhibit the highest transmittance, which reaches up to 82% at 780 nm, which is comparable to that of the LuAG single crystals grown by conventional Czochralski method [14]. At the same time, the transparent ceramics have excellent infrared transmittance (> 80% at 780–4950 nm), so it has potential application prospects in the fields of infrared windows, infrared thermal imagers, and infrared observers. When the heat-treated temperature is above or below 1100 ℃, the obtained samples all exhibit a lower light transmittance, especially in the visible to the NIR region. The reduced transmittance of the samples obtained

at 950 and 1000 ℃ could be assigned to the increased light scattering derived from the presence of the $LuAlO_3$ phase that is detected by the XRPD patterns in Fig. 1(b). Besides, the enhanced light scattering is observed in the ultraviolet and visible ranges when the heat-treated temperature is increasing, leading to the reduced transmittance of the samples obtained at 1200 ℃ and the opacity of the samples obtained at 1300 ℃. According to Rayleigh–Gans–Debye theory, this light scattering is mainly linked to the increase of the grain size resulting from the increased temperature.

In addition, the large refractive index difference between the Al_2O_3 secondary phase and the LuAG matrix inevitably leads to enhanced light scattering, so it is usually difficult to realize the high transparency of biphasic ceramics with both Al_2O_3 and LuAG phases. The reported Ce:LuAG–Al_2O_3 composite ceramics, e.g., composed of the micron-sized LuAG grains and Al_2O_3 grains, present a hazy appearance [41]. The LuAG–Al_2O_3 biphasic nanoceramics from the crystallization of the ALu28 bulk glass-based precursors, however, have managed to remain extremely transparent in visible light, which should be attributed to the weak scattering effect benefiting from its nano-sized grains, according to Rayleigh–Mie scaffolding theory. The as-prepared ceramic materials even exhibit good transparency after a heat treatment at 1100 ℃ for 72 h, as shown in Fig. S3 in the ESM. Furthermore, as presented in Fig. 3(b), the grains of the LuAG–Al_2O_3 biphasic ceramics crystallized from the ALu28 bulk glass-based precursors at 1300 ℃ grow with the heat-treated temperature rising. The grain growth mechanism is believed to be related to the coalescence effects among the grains, as observed in the YAG–Al_2O_3 transparent ceramics [39]. Consequently, a larger grain size results in the increased light scattering and the consequent complete opacity of the LuAG– Al_2O_3 ceramics obtained at 1300 ℃.

3. 2 Optical and scintillation properties of Ce:LuAG–Al_2O_3 nanoceramics

The transmittance spectra of the LuAG–Al_2O_3 nanoceramics doped with different Ce concentrations and obtained at 1100 ℃ are displayed in Fig. 5. The inset pictures show that all samples (ϕ3 mm × 0.8 mm in thickness) appear bright yellow, and their color gradually deepens with the increase of the Ce^{3+} concentration. All the LuAG–Al_2O_3 nanoceramics doped with Ce^{3+} exhibit lower transmittance than the ones without Ce^{3+} (Fig. 4). The distinct absorption at 450 nm corresponds to the 4f → $5d^1$ transition of Ce^{3+}, and this absorption increases with the increase of the Ce doping concentration. Besides, according to Rayleigh–Mie scaffolding theory, the nano-sized grains have stronger scattering effect on ultraviolet light than that on visible light. Therefore, the opacity to ultraviolet light results from the enhanced light scattering as well as the typical absorption (near 350 nm) corresponding to the 4f → $5d^2$ transition of Ce^{3+}.

The XEL spectra of (i) transparent LuAG–Al_2O_3 nanoceramics (ϕ3 mm × 0.8 mm in thickness) doped with different Ce concentrations and (ii) commercial $Bi_4Ge_3O_{12}$ (BGO) single crystals (10 mm × 10 mm × 10 mm) are recorded in Fig. 6. The XEL spectra indicate that the BGO single crystal produces a broad emission band peak at 480 nm under the X-ray excitation, which

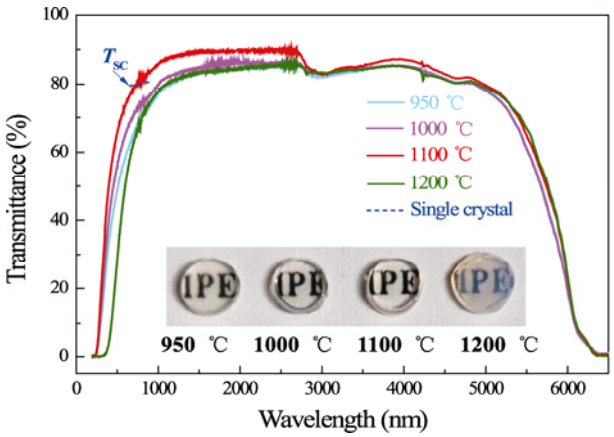

Fig. 4 In-line transmittance spectra of transparent materials (1.0 mm in thickness) crystalized from ALu28 glass-based precursors at 950, 1000, 1100, and 1200 ℃ for 2 h. The inset is their picture.

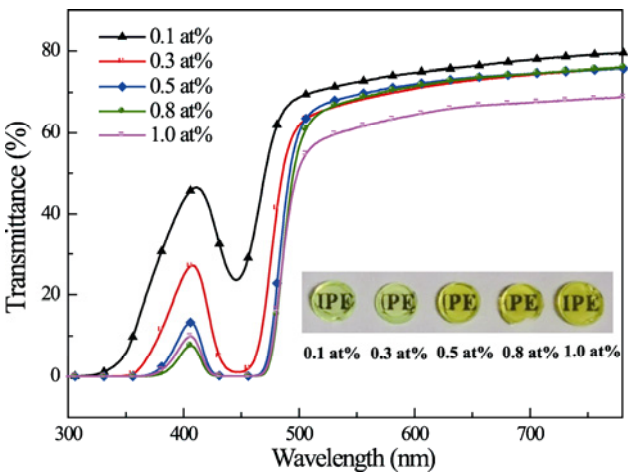

Fig. 5 Transmittance spectra of LuAG–Al_2O_3 nanoceramics (72 mol% Al_2O_3) doped with different Ce concentrations (1100 ℃, 2 h). The inset is their picture.

is consistent with Ref. [42]. The emission band of the transparent LuAG–Al_2O_3 nanoceramics doped with different Ce concentrations corresponds to the $5d^1 \rightarrow 4f$ transition of Ce^{3+}. As shown in the inset of Fig. 6, the emission peaks of the LuAG–Al_2O_3 nanoceramics show a slightly red shift with the increase of the Ce^{3+} doping concentration, on account of the splitting of 5d levels of Ce^{3+} [43]. The LuAG–Al_2O_3 nanoceramics doped with 0.3 at% Ce presents the strongest radioluminescence intensity peak at 520 nm, and its steady-state scintillator efficiency is about 2 times that of the commercial BGO single crystal. In addition, there is a weak ultraviolet emission band near 300 nm in the XEL spectrum of the LuAG–Al_2O_3 nanoceramics with 0.1 at% Ce doping concentration, which is attributed to the Lu_{Al} antisite defects that are ubiquitous in the LuAG single crystals and ceramics [18,27,44]. This shallow defect has been demonstrated to be the critical factor in producing slow scintillation tails [18–21]. These humble emission band peaks at 383, 420, and 770 nm may be associated with some uncontrolled impurities. The Ce^{3+} concentration has a certain positive effect on the inhibition of the Lu_{Al} antisite defects, but it is difficult to completely eliminate the Lu_{Al} antisite defects only by adjusting the Ce^{3+} concentration [19–21]. However, it is worth noting that the emission bands related to the Lu_{Al} antisite defects and other structural defects are completely undetectable in the XEL spectra of the resulting LuAG–Al_2O_3 nanoceramic materials with the Ce-doping concentration exceeding 0.1 at%. These results show that the low-temperature glass crystallization route is efficient for suppressing and reducing the appearance of the Lu_{Al} antisite defects in the LuAG-based transparent ceramics.

The TSL peaks corresponding to the Lu_{Al} antisite defects in the LuAG crystals appear in the temperature range of 120–200 K [18]. In addition to the Lu_{Al} antisite defects, other deeper traps may also reduce the light yields of the LuAG scintillation materials. It has been reported that because of the existence of the deep traps, at least 75% of the scintillation light produced in the LuAG:Ce ceramics is released in time of more than 1 μs [22]. Vedda *et al*. [45] demonstrated that the depth of the traps corresponding to the TSL bands between 300 and 700 K ranged from 1 to 1.9 eV. To further explore the existence of the deeper traps, the TSL measurements above room temperature of the LuAG–Al_2O_3 nanoceramics with different Ce doping concentrations were performed. The resulting TSL curves (300–780 K), as shown in Fig. 7, reveal that there are obvious TSL peaks near 350, 420, 550, and 695 K in the LuAG–Al_2O_3 nanoceramics with 0.1 at% Ce doping concentration. Predictably, not only the Lu_{Al} antisite defects and some possible structural defects but also some deep traps are generated in the LuAG–Al_2O_3 nanoceramics doped with 0.1 at% Ce. All TSL peak intensities of the LuAG–Al_2O_3 nanoceramics are significantly weakened with the increase of the Ce doping concentration, and particularly, the almost vanishing TSL peaks reflect the few deep traps in the LuAG–Al_2O_3 nanoceramics doped with 0.5 and 0.8 at% Ce. However, the TSL peaks are re-emerging when the Ce doping concentration increases to 1.0 at%. Thus, the Ce doping concentration plays an important role in impacting the TSL peak intensity above room temperature.

Figure 8(a) shows the pulse height spectra of the commercial BGO single crystal and transparent LuAG–Al_2O_3 nanoceramics doped with different Ce concentrations.

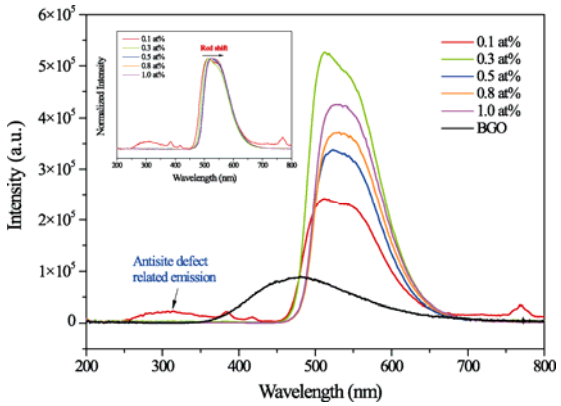

Fig. 6 XEL spectra of BGO single crystal and LuAG–Al_2O_3 nanoceramics (72 mol% Al_2O_3) doped with different Ce concentrations (1100 ℃, 2 h). The inset is the normalized XEL spectra.

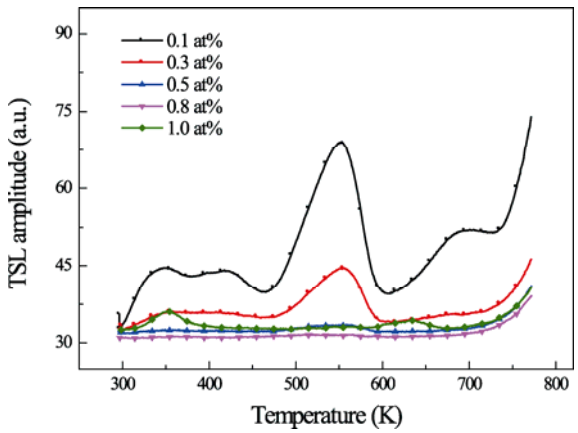

Fig. 7 TSL glow curves of LuAG–Al_2O_3 nanoceramics (72 mol% Al_2O_3) with different Ce concentrations (1100 ℃, 2 h) measured within the temperature range of 300–780 K.

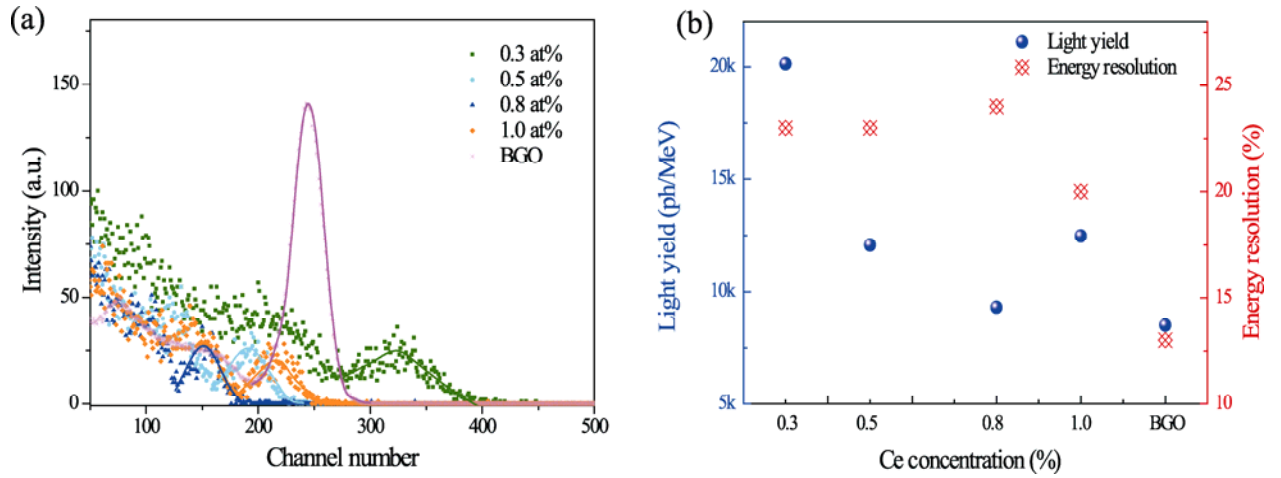

Fig. 8 (a) Pulse height spectra; (b) light yields and energy resolution of commercial BGO single crystal and LuAG–Al_2O_3 nanoceramics (72 mol% Al_2O_3) doped with different Ce concentrations (1100 ℃, 2 h).

The pulse signal of the LuAG–Al_2O_3 nanoceramics doped with 0.1 at% Ce is quite difficult to be detected due to the low light yield and very small dimension of ϕ3 mm × 0.8 mm. When the spectral sensitivity of the photocathode of the PMT is disregarded, light yields are given by the peak positions marked in pulse height spectra [27]. It appears that the peak positions of these LuAG–Al_2O_3 nanoceramics doped with different Ce concentrations are consistent with their XEL intensity. The ceramic materials doped with 0.3 at% Ce has the largest peak channel number, signifying that it has the highest light yield, which is about 133% of the light yield of the commercial BGO single crystal. In Ref. [46], the light yield of the Ce:LuAG scintillator ceramics fabricated using the solid-state reaction method is only about 60% of that of the BGO single crystal. Taking the light yield of the standard sample BGO single crystal as 8500 ph/MeV and the emission quantum efficiency of the PMT into consideration [47], the light yields of the LuAG–Al_2O_3 nanoceramics were estimated, as illustrated in Fig. 8(b). The light yield of the LuAG–Al_2O_3 nanoceramics doped with 0.3 at% Ce is estimated to be about 20,000 ph/MeV with shaping time of short 1 μs, which is inferior to that of Ce, Mg:LuAG (~25,000 ph/MeV) [23]. The smaller sizes of the LuAG–Al_2O_3 nanoceramic samples are likely to cause a part of the photons to be leaked, and thus not detected by the PMT. That is, actual light yields of the LuAG–Al_2O_3 nanoceramics probably far exceed the estimated values [48,49]. In addition, the energy resolution of the BGO single crystal and LuAG–Al_2O_3 nanoceramics doped with different Ce concentrations are presented in Fig. 8(b). The energy resolution of the LuAG–Al_2O_3 nanoceramics is inferior to that of the BGO single crystal. We expect that the LuAG–Al_2O_3 nanoceramics obtained by the crystallization of large-sized glass may lead to remarkable scintillation properties. Hot pressing sintering of small-sized amorphous materials near T_g appears as a promising solution to obtain the large- sized glass [50,51].

4 Conclusions

Highly transparent LuAG–Al_2O_3 nanoceramics were synthesized through the low-temperature (1100 ℃) glass crystallization of the ALu28 bulk glass. The resulting ceramics exhibit a density of 6.3 g/cm^3, and present a biphasic nanostructure of the LuAG nanocrystals separated by some Al_2O_3 domains. The dense LuAG–Al_2O_3 nanoceramics show almost perfect transparency in the visible and MIR regions. The in-line transmittance of this nanoceramic reaches up to 82% at 780 nm, at the same level as the LuAG single crystals. Moreover, the emission band related to the Lu_{Al} antisite defects is completely undetectable in the XEL spectra of the resulting LuAG–Al_2O_3 nanoceramic materials with the Ce-doping concentration varying from 0.3 to 1.0 at%. When the Ce doping concentration is 0.3 at%, the LuAG–Al_2O_3 nanoceramics demonstrate the highest light yield, estimated to be about 20,000 ph/MeV, with shaping time of short 1 μs. Thus, with higher light yields than those of the commercial BGO single crystals, these Ce:LuAG–Al_2O_3 nanoceramic materials can satisfy most scintillation-related applications. Therefore, the low-temperature glass crystallization route provides a

promising alternative for preparing the garnet-based transparent ceramic materials free of the antisite defects, which could further drive the development of the garnet-based transparent ceramic materials in the field of advanced scintillation applications, such as medical imaging and high-energy ray detection.

Acknowledgements

This work is financially supported by the National Natural Science Foundation of China (No. 51972304), Beijing Municipal Science & Technology Commission, Administrative Commission of Zhongguancun Science Park (No. Z221100006722022), the Project of Scientific Experiment on Chinese Manned Space Station, Chinese Academy of Sciences President's International Fellowship Initiative for 2021 (No. 2021VEA0012), and the Fundamental Research Funds for the Central Universities. This work has benefited from the electron microscopy facilities of the Platform MACLE-CVL, which was cofounded by the European Union and Centre-Val de Loire Region (FEDER).

Electronic Supplementary Material

Supplementary material is available in the online version of this article at https://doi.org/10.26599/JAC.2023.9220681.

References

[1] Nikl M, Yoshikawa A. Recent R&D trends in inorganic single-crystal scintillator materials for radiation detection. *Adv Opt Mater* 2015, **3**: 463–481.

[2] Xu X, Lebbou K, Moretti F, *et al*. Ce-doped LuAG single-crystal fibers grown from the melt for high-energy physics. *Acta Mater* 2014, **67**: 232–238.

[3] Hu ZW, Cao MQ, Chen HH, *et al*. The role of air annealing on the optical and scintillation properties of Mg co-doped Pr:LuAG transparent ceramics. *Opt Mater* 2017, **72**: 201–207.

[4] Nikl M, Yoshikawa A, Kamada K, *et al*. Development LuAG-based scintillator crystals—A review. *Prog Cryst Growth Ch* 2013, **59**: 47–72.

[5] Chewpraditkul W, Sreebunpeng K, Nikl M, *et al*. Comparison of $Lu_3Al_5O_{12}$:Pr^{3+} and $Bi_4Ge_3O_{12}$ scintillators for gamma-ray detection. *Radiat Meas* 2012, **47**: 1–5.

[6] Chen XP, Hu ZW, Dai JW, *et al*. The influence of air annealing on the microstructure and scintillation properties of Ce,Mg:LuAG ceramics. *J Am Ceram Soc* 2019, **102**: 1805–1813.

[7] Ma WQ, Jiang BX, Feng XQ, *et al*. On fast LuAG:Ce scintillation ceramics with Ca^{2+} co-dopants. *J Am Ceram Soc* 2021, **104**: 966–973.

[8] Ikesue A, Aung YL. Ceramic laser materials. *Nat Photonics* 2008, **2**: 721–727.

[9] Messing GL, Stevenson AJ. Toward pore-free ceramics. *Science* 2008, **322**: 383–384.

[10] Hinklin TR, Rand SC, Laine RM. Transparent, polycrystalline upconverting nanoceramics: Towards 3-D displays. *Adv Mater* 2008, **20**: 1270–1273.

[11] Van Eijk CW. Inorganic scintillators in medical imaging. *Phys Med Biol* 2002, **47**: R85–R106.

[12] Gerasymov I, Nepokupnaya T, Boyarintsev A, *et al*. GAGG:Ce composite scintillator for X-ray imaging. *Mater* 2020, **109**: 110305.

[13] Yanagida T, Fujimoto Y, Yokota Y, *et al*. Comparative study of transparent ceramic and single crystal Ce doped LuAG scintillators. *Radiat Meas* 2011, **46**: 1503–1505.

[14] Yanagida T, Fujimoto Y, Kamada K, *et al*. Scintillation properties of transparent ceramic Pr:LuAG for different Pr concentration. *IEEE Trans Nucl Sci* 2012, **59**: 2146–2151.

[15] Hu C, Feng XQ, Li J, *et al*. Role of Y admixture in $(Lu_{1-x}Y_x)_3Al_5O_{12}$:Pr ceramic scintillators free of host luminescence. *Phys Rev Appl* 2016, **6**: 064026.

[16] Wu YT, Luo ZH, Jiang HC, *et al*. Single crystal and optical ceramic multicomponent garnet scintillators: A comparative study. *Nucl Instrum Meth A* 2015, **780**: 45–50.

[17] Dorenbos P. Fundamental limitations in the performance of Ce^{3+}-, Pr^{3+}-, and Eu^{2+}-activated scintillators. *IEEE Trans Nucl Sci* 2010, **57**: 1162–1167.

[18] Nikl M, Mihokova E, Pejchal J, *et al*. The antisite Lu_{Al} defect-related trap in $Lu_3Al_5O_{12}$:Ce single crystal. *Phys Status Solidi B* 2005, **242**: R119–R121.

[19] Liu SP, Mares JA, Babin V, *et al*. Composition and properties tailoring in Mg^{2+} codoped non-stoichiometric LuAG:Ce,Mg scintillation ceramics. *J Eur Ceram Soc* 2017, **37**: 1689–1694.

[20] Nikl M, Kamada K, Babin V, *et al*. Defect engineering in Ce-doped aluminum garnet single crystal scintillators. *Cryst Growth Des* 2014, **14**: 4827–4833.

[21] Nikl M, Pejchal J, Mihokova E, *et al*. Antisite defect-free $Lu_3(Ga_xAl_{1-x})_5O_{12}$:Pr scintillator. *Appl Phys Lett* 2006, **88**: 141916.

[22] Liu SP, Feng XQ, Zhou ZW, *et al*. Effect of Mg^{2+} co-doping on the scintillation performance of LuAG:Ce ceramics. *Phys Status Solidi-R* 2014, **8**: 105–109.

[23] Liu SP, Mares JA, Feng XQ, *et al*. Towards bright and fast $Lu_3Al_5O_{12}$:Ce,Mg optical ceramics scintillators. *Adv Opt Mater* 2016, **4**: 731–739.

[24] Zhang JY, Luo ZH, Liu YF, *et al*. Cation-substitution induced stable GGAG:Ce^{3+} ceramics with improved optical and scintillation properties. *J Eur Ceram Soc* 2017, **37**: 4925–4930.

[25] Zorenko Y, Gorbenko V, Konstankevych I, *et al*. Single-crystalline films of Ce-doped YAG and LuAG phosphors: Advantages over bulk crystals analogues. *J Lumin* 2005, **114**: 85–94.
[26] Zorenko Y, Gorbenko V, Voloshinovskii A, *et al*. Exciton-related luminescence in LuAG:Ce single crystals and single crystalline films. *Phys Status Solidi A* 2005, **202**: 1113–1119.
[27] Hu ZW, Chen XP, Chen HH, *et al*. Suppression of the slow scintillation component of Pr:$Lu_3Al_5O_{12}$ transparent ceramics by increasing Pr concentration. *J Lumin* 2019, **210**: 14–20.
[28] Ling JR, Zhou YF, Xu WT, *et al*. Red-emitting YAG:Ce, Mn transparent ceramics for warm WLEDs application. *J Adv Ceram* 2020, **9**: 45–54.
[29] Wang HM, Huang ZY, Qi JQ, *et al*. A new methodology to obtain the fracture toughness of YAG transparent ceramics. *J Adv Ceram* 2019, **8**: 418–426.
[30] Chen XP, Hu ZW, Dai JW, *et al*. Fabrication and optical properties of cerium doped $Lu_3Ga_3Al_2O_{12}$ scintillation ceramics. *Opt Mater* 2018, **85**: 121–126.
[31] Hua H, Feng SW, Ouyang ZY, *et al*. YAGG:Ce transparent ceramics with high luminous efficiency for solid-state lighting application. *J Adv Ceram* 2019, **8**: 389–398.
[32] Xu J, Wang J, Gong YX, *et al*. Investigation of an LuAG:Ce translucent ceramic synthesized via spark plasma sintering: Towards a facile synthetic route, robust thermal performance, and high-power solid state laser lighting. *J Eur Ceram Soc* 2018, **38**: 343–347.
[33] Pan LJ, Jiang BX, Fan JT, *et al*. Preparation of LuAG powders with single phase and good dispersion for transparent ceramics using co-precipitation method. *Materials* 2015, **8**: 5363–5375.
[34] Milisavljevic I, Pitcher MJ, Li JQ, *et al*. Crystallization of glass materials into transparent optical ceramics. *Int Mater Rev* 2022, 1–29.
[35] Alahraché S, Al Saghir K, Chenu S, *et al*. Perfectly transparent $Sr_3Al_2O_6$ polycrystalline ceramic elaborated from glass crystallization. *Chem Mater* 2013, **25**: 4017–4024.
[36] Allix M, Alahrache S, Fayon F, *et al*. Highly transparent $BaAl_4O_7$ polycrystalline ceramic obtained by full crystallization from glass. *Adv Mater* 2012, **24**: 5570–5575.
[37] Boyer M, Yang XY, Carrion AJF, *et al*. First transparent oxide ion conducting ceramics synthesized by full crystallization from glass. *J Mater Chem A* 2018, **6**: 5276–5289.
[38] Boyer M, Carrion AJF, Ory S, *et al*. Transparent polycrystalline $SrREGa_3O_7$ melilite ceramics: Potential phosphors for tuneable solid state lighting. *J Mater Chem C* 2016, **4**: 3238–3247.
[39] Ma XG, Li XY, Li JQ, *et al*. Pressureless glass crystallization of transparent yttrium aluminum garnet-based nanoceramics. *Nat Commun* 2018, **9**: 1175.
[40] Zhang Y, Ma XG, Li XY, *et al*. Crystallization kinetics of Al_2O_3–26mol% Y_2O_3 glass and full crystallized transparent $Y_3Al_5O_{12}$-based nanoceramic. *J Eur Ceram Soc* 2021, **41**: 1557–1563.
[41] Zhang Q, Zheng RL, Ding JY, *et al*. High lumen density of Al_2O_3–LuAG:Ce composite ceramic for high-brightness display. *J Am Ceram Soc* 2021, **104**: 3260–3268.
[42] Luo ZH, Jiang HC, Jiang J, *et al*. Microstructure and optical characteristics of Ce:$Gd_3(Ga,Al)_5O_{12}$ ceramic for scintillator application. *Ceram Int* 2015, **41**: 873–876.
[43] Wu HY, Yang C, Zhang ZX, *et al*. Photoluminescence and thermoluminescence of Ce^{3+} incorporated $Y_3Al_5O_{12}$ synthesized by rapid combustion. *Optik* 2016, **127**: 1368–1371.
[44] Liu SP, Feng XQ, Mares JA, *et al*. Optical, luminescence and scintillation characteristics of non-stoichiometric LuAG: Ce ceramics. *J Lumin* 2016, **169**: 72–77.
[45] Vedda A, di Martino D, Martini M, *et al*. Thermoluminescence of Zr-codoped $Lu_3Al_5O_{12}$:Ce crystals. *Phys Status Solidi A* 2003, **195**: R1–R3.
[46] Liu SP, Feng XQ, Shi Y, *et al*. Fabrication, microstructure and properties of highly transparent Ce^{3+}:$Lu_3Al_5O_{12}$ scintillator ceramics. *Opt Mater* 2014, **36**: 1973–1977.
[47] Mao RH, Zhang LY, Zhu RY. Optical and scintillation properties of inorganic scintillators in high energy physics. *IEEE Trans Nucl Sci* 2008, **55**: 2425–2431.
[48] Zhou TY, Hou C, Zhang L, *et al*. Efficient spectral regulation in Ce:$Lu_3(Al,Cr)_5O_{12}$ and Ce:$Lu_3(Al,Cr)_5O_{12}$/Ce:$Y_3Al_5O_{12}$ transparent ceramics with high color rendering index for high-power white LEDs/LDs. *J Adv Ceram* 2021, **10**: 1107–1118.
[49] Hua H, Feng SW, Ouyang ZY, *et al*. YAGG:Ce transparent ceramics with high luminous efficiency for solid-state lighting application. *J Adv Ceram* 2019, **8**: 389–398.
[50] Han JJ, Wang Z, Li JQ, *et al*. Large-sized La_2O_3–TiO_2 high refractive glasses with low SiO_2 fraction by hot-press sintering. *Int J Appl Glass Sci* 2019, **10**: 371–377.
[51] Li RY, Li XY, Li JQ, *et al*. Large-sized La_2O_3–TiO_2–SiO_2 amorphous oxide fabricated by hot press sintering. *J Inorg Mater* 2017, **32**: 851–856. (in Chinese)